IEEE Access
Multidisciplinary | Rapid Review | Open Access Journal

Received June 1, 2019, accepted June 27, 2019, date of publication July 2, 2019, date of current version July 19, 2019.

Digital Object Identifier 10.1109/ACCESS.2019.2926091

MEMS Non-Magnetic Electric Heating Chip for Spin-Exchange-Relaxation-Free (SERF) Magnetometer

LIANG XIAOYANG[1], LIU ZHANCHAO[1,2], DIE HU[1], WU WENFENG[1], JIA YUCHEN[1], AND FANG JIANCHENG[1]

[1]School of Instrumentation and Optoelectronics Engineering, Beihang University, Beijing 100191, China
[2]Beijing Advanced Innovation Center for Big Data-Based Precision Medicine, Beihang University, Beijing 100191, China

Corresponding author: Liu Zhanchao (liuzhanchao@hotmail.com)

This work was supported in part by the National Natural Science Foundation of China (NSFC) under Grant 61421063 and Grant 61703021, and in part by the National Key Research and Development Program of China under Grant 2016YFB0501600.

ABSTRACT The alkali metal atoms in spin-exchange-relaxation-free (SERF) atomic magnetometers require high temperature and non-magnetic environment. Increasing the temperature of the alkali metal atoms causes higher atomic density, which can enhance the intensity of the output signal. However, heating current introduces additional magnetic flux density and unexpected gradient, which will reduce the device's sensitivity. Therefore, it is necessary to develop a non-magnetic heating chip for the SERF magnetometer. In this paper, a new design for non-magnetic heating chips, fabricated by the microelectromechanical system (MEMS) technique with platinum deposited on the semiconductor substrates, is proposed. The designed chip is composed of two layers of the same serpentine-shaped resistors to suppress the magnetic flux density, with an insulation layer in the middle. There are two sets of wires in each layer used as a thermometer resistor and a heating resistor forming a feedback loop of temperature control. The simulation results show that the magnetic effect between the layers can be reduced by four orders than in one layer. The experimental results show that the temperature coefficient of resistance (TCR) is approximately 0.224%/°C. The consistency of the resistance is better than 97.7%. The fluctuation of temperature at 110 °C is under 10 mK. The magnetic flux density introduced by the current in the z-direction is 0.22146 nT/mA.

INDEX TERMS Non-magnetic electric heating chip, Micro-electro-mechanical system, double spiral structure, SERF magnetometer.

I. INTRODUCTION

Common magnetometers include fluxgate magnetometers, Superconducting Quantum Interference Devices (SQUID), Giant Magneto-Resistance (GMR) Magnetometers and Optically Pumped Magnetometers (OPM) [1]. The fluxgate magnetometer has a simple measurement principle, but the measurement sensitivity is difficult to improve. SQUID has high measurement sensitivity, but the requirement of cryogenic environment means a complex structure [2]. GMR magnetometers is a portable, low-cost and low-power magnetometer based on thin-film technology [3]. In recent years, using the atom as a sensitive medium to measure the magnetic flux density has been rapidly developed. Optically Pumped Magnetometers (OPM) provide a highly sensitive measure of the local magnetic field using optical pumping and probing of alkali atoms [4]. The most sensitive atomic optical magnetometer is the Spin-Exchange-Relaxation-Free (SERF) Magnetometers whose demonstrated sensitivity exceeds 10^{-15} T/$\sqrt{Hz}$ [5]. Compared with traditional types of magnetic measurement devices, SERF magnetometers based on the atomic spin effect offer improvements in sensitivity, volume and other characteristics [6]–[9]. Magnetic flux density detection of SERF magnetometer is obtained by detecting alkali-metal electron spin. Increasing the temperature of alkali metal atoms makes higher atomic density which can enhance the intensity of the output signal. For the purpose of increasing the atomic density, the alkali metal vapor cell

The associate editor coordinating the review of this manuscript and approving it for publication was Sanket Goel.

working as the core of the atomic devices should be heated to 100-200°C, depending on the kind of alkali metal [6]. Temperature fluctuation will cause changes in multiple parameters including the atomic density, the relaxation rate and the polarization. It is necessary to measure and control the temperature accurately [10]. The typical power needed for a SERF magnetometer are mostly used for heating. The power is about 1 mW – 50 W dependent on the cell size, physics package and the coating around the physics package [11], [12]. However, heating current will introduce an extra magnetic flux density. As the atomic devices are extremely sensitive to the magnetic interference, traditional heating method reduces the sensitivity of the magnetometer. Therefore, it is necessary to develop a non-magnetic heating chip for the SERF magnetometer. Besides, miniaturized design of magnetometer requires highly integrated heating chips.

Princeton University firstly applied flowing hot air to heat the vapor cell, which is absolutely non-magnetic and easy to achieve a high heating power [13], Then Princeton University applied fine pair of winding resistance wire to heat the cell [12], [14]. The research group in University of Wisconsin–Madison put two meander resistor heaters back to back and wiring the resistors in anti-series helped suppress the magnetic flux density produced by heater currents. Each cell uses two sets of these heating pairings, wired in series to reduce the magnetic flux density further. The spacing between metal lines is on the order of millimeter which can be further reduction by the techniques of micro electro mechanical systems to enhance the suppression effect [10]. In the chip-scale atomic magnetometer developed by National Institute of Standards and Technology, the design of the indium tin-oxide (ITO) heater employed a double meandering resistive track. Thanks to the techniques of micro electro mechanical systems (MEMS), it is separated by only 10 μm from the path of the input current to the return path of the current, bringing better magnetic flux density suppression effect. However, only the heating function is realized, the platinum resistance needs to be combined to measure the temperature [15]. Northrop Grumman Navigation Systems Division develops a kind of temperature system including multi-layer conductors patterned to conduct currents in directions that generate 2^N multipole magnetic moments, which interact to suppress the magnetic flux density [16].

In this paper, a non-magnetic electric heating chip is developed with MEMS technology. Magnetic simulation is conducted to study the structure, and Platinum (Pt) is chosen as the material of the resistance wire. The integration of heating and temperature measurement makes a great contribution to the temperature control system and the miniaturization of physics package for SERF magnetometers. The experiment result shows that the magnetic flux density introduced by the current in the Z direction is only 0.22146 nT/mA, which is close to the simulation result. The temperature coefficient of resistance (TCR) test are also calibrated to obtain the relationship between resistance and temperature.

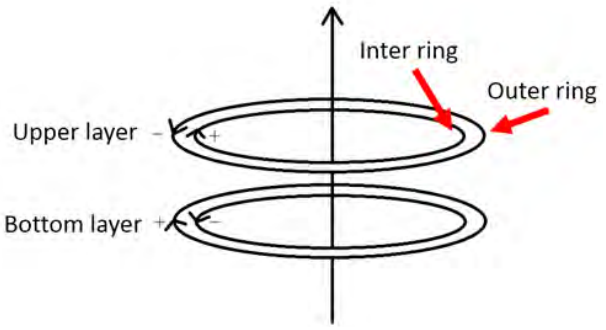

FIGURE 1. Simplified model of the heating coils.

II. SENSOR DESIGN AND FABRICATION

A. OVERALL STRUCTURE DESIGN

The magnetic flux density model is simulated to give guidance on the setting of parameters such as the number of layers, the number of coils, and the distance between two layers of metal. The heating chip is composed of heating coils and thermometer coils. The current in the heating coils is larger than the slight current in the temperature measurement coils. Therefore, only the circle part of the heating coils is considered to simplify the model, as shown in Fig. 1. The simplified model is composed of two layers. The currents in the upper layer and the bottom layer are equal with opposite directions. Each layer includes an inter ring and an outer ring with different directions of heating current.

The Biot-Savart Law describes the magnetic flux density excited by the unit current at any point P in space.

$$B = \int \frac{\mu_0}{4\pi} \frac{Id\vec{l} \times \vec{r}}{r^2} \tag{1}$$

According to the Biot-Savart Law, the magnetic flux density in the axial direction generated by a circular coil is given by:

$$B = \frac{N\mu_0 IR^2}{2(x^2 + R^2)^{3/2}} \tag{2}$$

where B is the magnetic flux density, N is the number of coil turns, μ_0 is permeability of vacuum, I is the current which is set to 100 mA, R is the radius of the coil which is set to 975 μm for the inner ring and 1175 μm for the outer ring, and x is the distance in the axial direction and the spacing between two layers is set as 300 nm.

1) MAGNETIC FLUX DENSITY GENERATED BY BOTTOM LAYER COILS

Because the structures of top layer and bottom layer are the same, firstly only the magnetic flux density generated by the bottom layer coils, including the inner ring and the outer ring, is considered. Curves of generated magnetic flux density by the inner coil, the outer coil, and both coils in the range of $x = [0, 10]$, are plotted in Fig. 2 (a), and for better observation the range of $x = [6, 8]$ is magnified in Fig. 2(b). At the center of the vapor cell of the atomic instrument, $z = 7$ mm, the magnetic flux density generated by each coil is

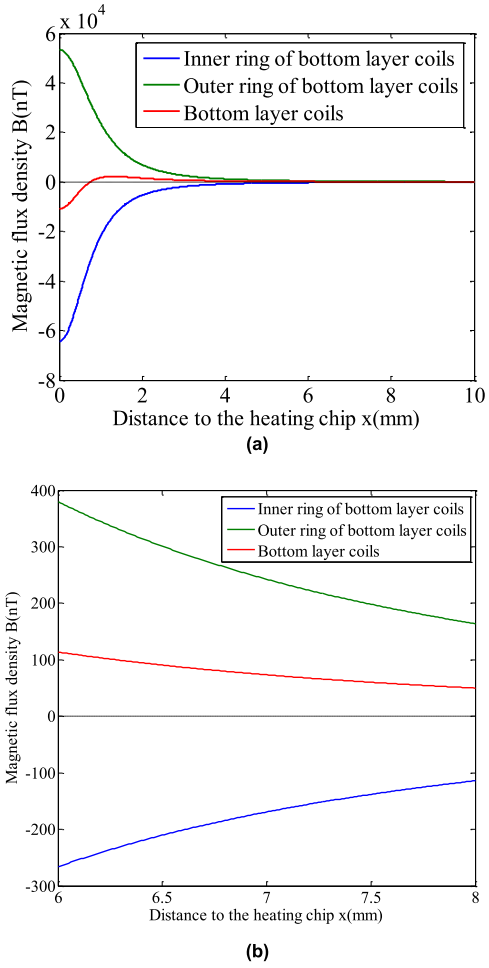

FIGURE 2. Magnetic flux density generated by bottom layer coils (a) x = [0, 10]. (b) x = [6, 8].

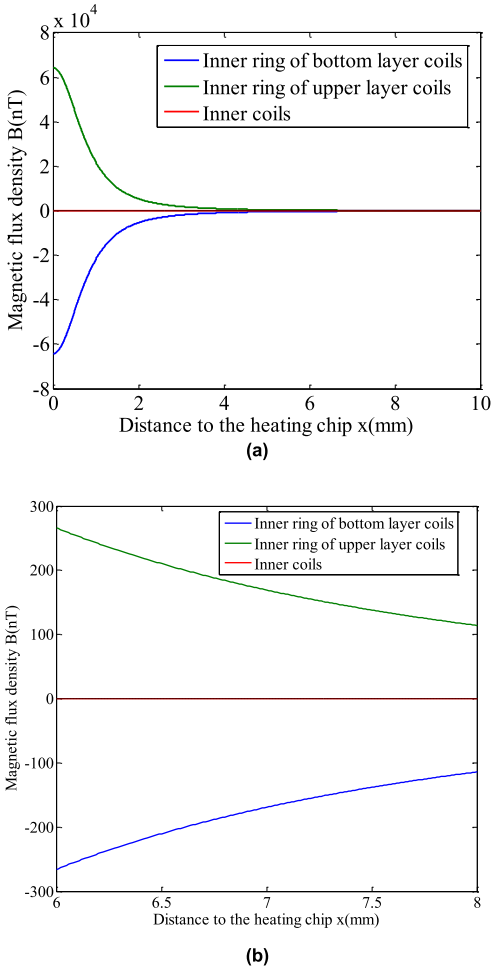

FIGURE 3. Magnetic flux density generated by inner coils (a) x = [0, 10]. (b) x = [6, 8].

approximately 232.7 nT and −162.2 nT. The total magnetic flux density generated by the bottom layer including the inner ring and the outer ring is 70.5 nT, which is 2 - 3 times smaller than the magnetic flux density from one coil.

2) MAGNETIC FLUX DENSITY GENERATED BY INNER COILS

The currents of the upper and bottom resistor wires of the inner ring are calculated, and the magnetic flux densities generated by the two resistance wires spaced at 300nm are almost coincident. Curves of generated magnetic flux densities by the upper coil, the bottom coil, and both coils in the range of x = [0, 10], are plotted in Fig. 3 (a), and for better observation the range of x = [6, 8] is magnified in Fig. 3 (b). At the center of the cell, the magnetic flux density generated by the upper inner coil and the bottom inner coil are approximately 162.3 nT and −162.2 nT, and only 0.03364 nT after elimination. The total magnetic flux density is reduced by 4 orders of magnitude.

Comparing the magnetic flux density simulation diagrams in one layer and between layers, the magnetic flux density suppression in one layer can be reduced by about 2 - 3 times. However, the suppression effect between layers can be reduced by 4 orders of magnitude. The reason is that the interval between layers can be fabricated as thin as nanoscale, but the gap between coils in a layer is microscale. In general, magnetic flux density suppression mainly depends on mutual elimination between the two layers, which requires alignment accuracy of the two metal layers.

3) MAGNETIC FLUX DENSITY GENERATED BY ALL COILS

When all coils in both upper and bottom layers are considered, curves of total generated magnetic flux density in the range of x = [0, 10], are plotted in Fig. 4 (a), and for better observation the range of x = [6, 8] is magnified in Fig. 4 (b). The magnetic flux density generated in the center of the cell is approximately 0.0142 nT, which shows a good magnetic flux density suppression effect.

4) MAGNETIC FLUX DENSITY WITH DIFFERENT SPACING BETWEEN TWO LAYERS

In the simplified model, the distance between double-layered resistor wires varies from 100 nm to 500 nm. As shown in Fig. 5, when the thickness of the insulating layer is larger, the residual magnetic flux density at the point 7 mm away

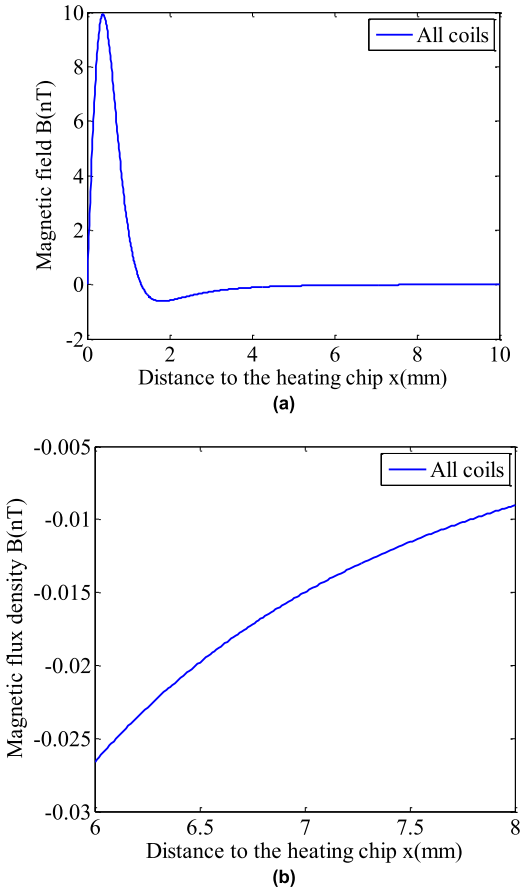

FIGURE 4. Magnetic flux density generated by all coils (a) x = [0, 10]. (b) x = [6, 8].

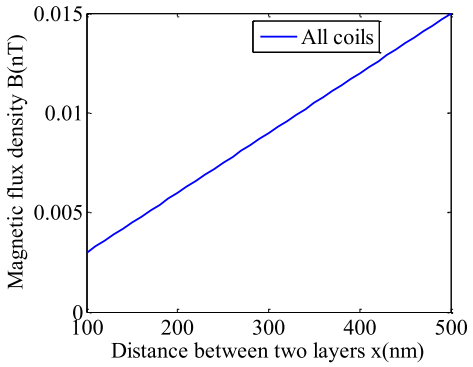

FIGURE 5. Magnetic flux density with different spacing between two layers.

consequently becomes larger. However, the insulation layer needs a certain thickness to ensure the insulation performance to avoid breakdown when the voltage is large. In this paper, an empirical value of 300 nm is selected.

5) MAGNETIC FLUX DENSITY WITH DIFFERENT SPACING BETWEEN TWO LAYERS

The alignment marks make the two layers aligned while the two layers cannot be in exactly the same position. So, the mismatch between two layers due to process error should be considered. Usually the alignment error is less than 1 μm,

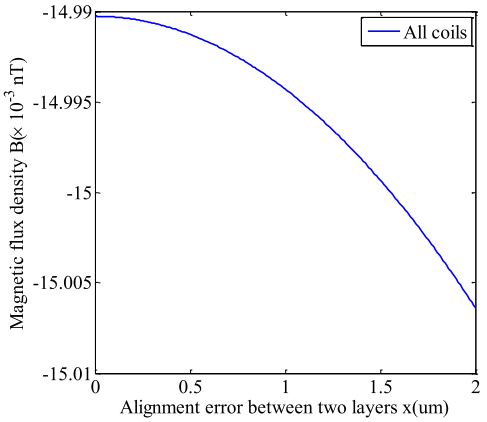

FIGURE 6. Magnetic flux density in Z axis with different alignment error between two layers.

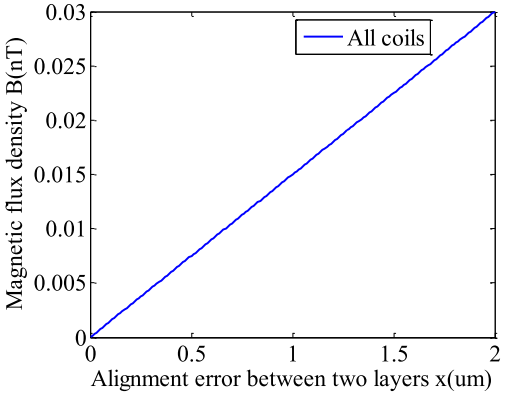

FIGURE 7. Magnetic flux density in Y axis with different alignment error between two layers.

so the range from 0 to 2 μm is simulated. As shown in Fig. 6, the absolute value of the residual magnetic flux density in Z axis increases slightly with the alignment error between two layers. As shown in Fig. 7, the absolute value of the residual magnetic flux density in Y axis increases slowly with the alignment error between two layers. As a simple conclusion, the alignment error has a limited impact on the magnetic flux density. However, alignment errors still should be avoided.

B. MATERIAL SELECTION AND RESISTANCE CALCULATION

Platinum has long been considered as a good resistor material used for measuring temperature because of its chemical inertness and physical stability. Moreover, platinum has a high temperature coefficient of resistance (TCR), which means higher sensitivity to temperature with the same resistance. The resistivity is linearly related to the temperature within a large range of −200°C - 1200°C, which contributes to a more accurate temperature measurement [17], [18]. Therefore, Pt is selected as the material of the resistor.

In order to avoid breakdown of the heating chip, the magnitude of sinusoidal heating voltage effective value is set to 30V. The power consumption required for heating is about 1 - 2W, therefore the heating resistance should be around 200Ω.

The relationship between the resistivity of the platinum resistor and the temperature in the range of 0°C - 850°C is,

$$w_t = R_t/R_0 = 1 + At + Bt^2 \tag{3}$$

where R_t is the resistance under t °C,R_0 is the resistance under 0 °C, $A = 3.9083 \times 10^{-3}°C^{-1}$, $B = -5.7750 \times 10^{-7}°C^2$. Thus, at the temperature of 20°C and 110°C,

$$w_{20} = 1 + 3.9083 \times 10^{-3} \times 20 - 5.7750 \times 10^{-7} \times 20^2 = 1.077935 \tag{4}$$

$$w_{110} = 1 + 3.9083 \times 10^{-3} \times 110 - 5.7750 \times 10^{-7} \times 110^2 = 1.422925 \tag{5}$$

The vapor cell should be heated to 110°C when the magnetometer is working. According to the resistivity under 20°C, $\rho_{20} = 1.05 \times 10^{-7}\Omega \cdot m$, it is easy to calculate the resistivity under 110°C.

$$\rho_{110} = \frac{\rho_{20}}{w_{20}} \times w_{110} = \frac{1.05 \times 10^{-7}}{1.077935} \times 1.422925 = 1.38605 \times 10^{-7}\Omega \cdot m \tag{6}$$

In order to obtain a suitable resistance of the heating chip, which is 200Ω in this paper, the width, length, and thickness of the wires are further designed according to the platinum resistivity.

C. COIL STRUCTURE

In each layer, the inner ring resistor wire is used for heating. Under the same breakdown voltage, the smaller resistance reaches the higher heating power. Thus, the inner wire should be wide and short to obtain the faster heating effect. However, the outer ring wire, working as the temperature sensor, should be a large resistance to improve the sensitivity to temperature changes. Therefore, the inner ring wire is made of a 150 μm wide strip of platinum, reaching a resistance of 200 Ω, whereas the outer ring is made of 10 laps of wires (5 pairs) with the width of 14 μm. The long and thin resistive track makes the resistance reach 10 kΩ.

Fig. 8 shows the layout of upper and bottom platinum resistors overlap, where red is the bottom resistor track, blue is the upper resistor track. The two platinum resistors are only slightly different at the lead. Therefore, the identical main coil structure in both layer ensures mutual elimination of magnetic flux densities. In each layer, the inner heating resistor wire and the outer temperature sensor wire are both even-numbered turns with meandering track.

Fig. 9 shows the current directions in two layers of platinum resistor. Red is the bottom resistor track, blue is the upper resistor track, and purple is the overlap. Take the inner heating coil as an example, the external current first flows in from the bottom lead at A. After entering the bottom coil, it flows to the connection between two layers at B and turns into the top metal layer through the hole in electrical insulation layer (not shown in Fig. 9). It then flows in opposite

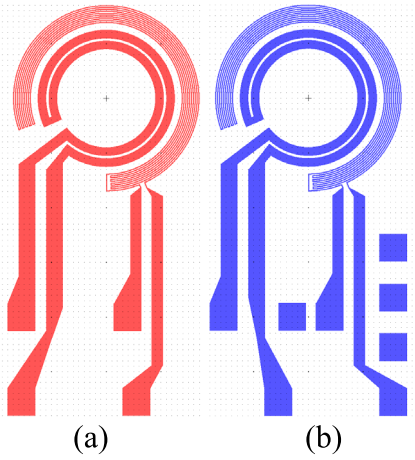

FIGURE 8. The layout of resistors on the upper and bottom layers (a) upper (b) bottom.

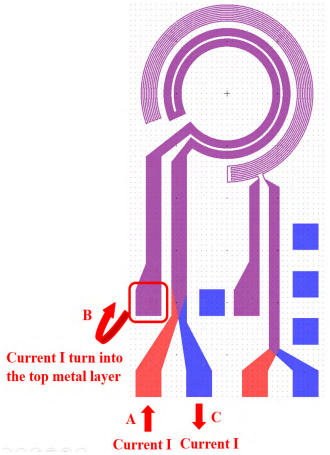

FIGURE 9. Layout of overlap resistors on the upper and bottom layers.

direction with the bottom coil, and finally flows out from the top lead at C.

The current through the upper and bottom platinum resistors generates the same magnetic flux density with opposite directions, so the magnetic flux density could be mostly eliminated. The direction of the outer ring current is the same.

D. SENSOR FABRICATION

1) HEATING CHIP STRUCTURE

MEMS technology is utilized to fabricate the heating chip, which is beneficial to miniaturization of the atomic device physics package. The structure of the chip is designed to be two layers of the same serpentine shaped platinum resistor with the insulation layer in the middle, as shown in Fig. 10.

2) FABRICATION PROCESS

Fabrication process of the heating chip starts with a 500 μm silicon wafer coated with 1 μm of thermally oxidized silicon. The process is listed as follow:

1) Cover the substrate with photoresist and pattern the photoresist using the mask. Etch the thermally oxidized silicon as deep as the metal thickness. Sputter the first layer of metal and

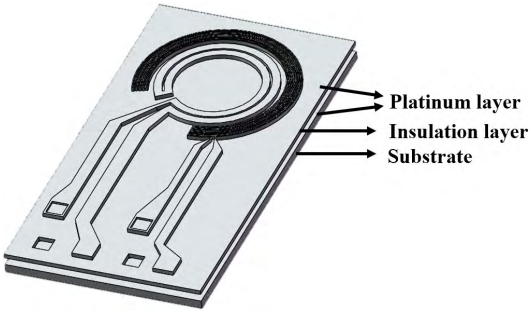

FIGURE 10. Double spiral structure of the heating chip.

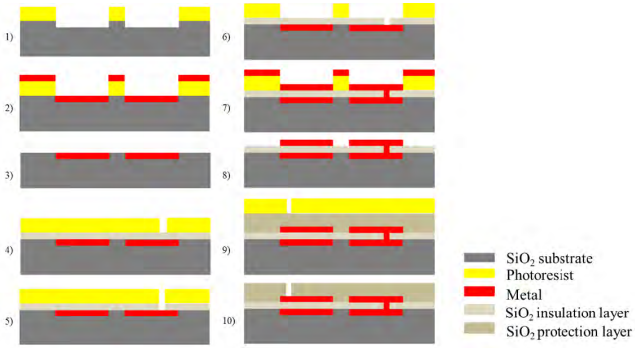

FIGURE 11. Heating chip structure diagram.

FIGURE 12. Contrast diagram of heating film substrate (a) not etched (b) etched.

bury the metal in the groove. Remove excess metal by lifting off the photoresist from the wafer, forming a whole plane on the upper surface, as Fig. 11 (1-3) show.

2) Deposit silicon oxide by Plasma Enhanced Chemical Vapor Deposition (PECVD) as the insulation layer. Etch the insulation layer at the connection area so that the bottom metal is exposed through the hole, as Fig. 11 (4-5) show.

3) Sputter and pattern the upper layer metal through the same lift-off process with step 1. The two layers of metal are connected through the hole in the insulation layer, so the main structure of the heating chip is completed, as Fig. 11 (6-8) show.

4) Deposit a thick SiO_2 protection layer by PECVD and expose the metal pads by etching the protection layer, to provide external electrical connections, as Fig. 11 (9-10) show.

It should be noted that if the first layer of metal is grown directly in step 1 without etching, as shown in Fig. 12 (a), the entire surface will have a certain height difference, which will make the insulation layer not smooth. As a result, the insulation performance and growth quality of upper metal will decrease, causing higher rate of defective products. Only if the thermally oxidized silicon layer is etched before the metal is deposited, the metal can be precisely embedded in the groove, as Fig. 12 (b) shows.

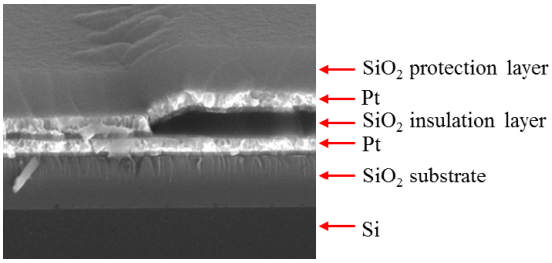

FIGURE 13. SEM image of the side elevation for the connection area.

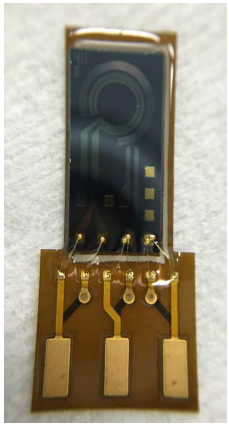

FIGURE 14. Heating chip physics package.

In addition, the high stress level in the Pt thin film weakens the adhesion with SiO_2, so the Cr, Pt, and Ti are deposited in series where Cr and Ti work as the adhesion layers.

3) CONNECTION AREA

Fig. 13 is the side elevation picture of connection area photographed by scanning electron micrographs (SEM). The bottom black part is the Si substrate, the gray part is the thermally oxidized silicon layer, the white part is the metal Pt, and the black part between metal Pt is the insulating layer of SiO_2. At the top is the protection layer of SiO_2.

It can be seen that on the right side of the SEM image, two metal layers are separated by the insulation layer, whereas on the left side of the SEM image, two Pt layers are bonded together to achieve effective conduction. In the connection area, the current can flow from the bottom coil into the upper coil in a reversed direction to suppress the magnetic flux density.

4) PHYSICS PACKAGE

After fabrication, the heating chip was bonded to the polyimide substrate. The pads on the heating chip and the substrate were connected by the gold wire bonding. The gold wires were protected by the UV glue which has a similar coefficient of thermal expansion, as shown in Fig. 14.

III. EXPERIMENT

A. RESISTANCE MEASUREMENT

Once the fabrication of heating chips was completed, the heating chips with short or open circuit were removed.

TABLE 1. Resistance test results of heating chips.

No.	Heating coil/Ω	Temperature sensing coil/Ω
1	224.3	10.61k
2	225.7	10.70k
3	224.3	10.75k
4	224.1	10.63K
5	220.7	10.53k

5 chips were extracted and their resistances of heating coils and temperature sensing coil were tested at room temperature (26°C). The test results are shown in Table 1.

The consistency of fabricated resistances was better than 97.7%. The difference between the designed resistance and the actual measured resistance was caused by the gap between the obtained resistivity by PECVD and the resistivity of bulk material. It was also affected by diffusion of adhesion layer into metal. Moreover, the lead resistance will also increase the measured resistance.

B. TEMPERATURE CALIBRATION

It is necessary to know the precise temperature corresponding to the measured resistance value while the heating chip is working in the system. Therefore, a calibration examination of several temperature points was conducted to obtain the relationship between resistance and temperature.

1) CALIBRATION EXPERIMENT SETUP

The heating chip and an industry-standard platinum resistor were placed in a thermostat at the same time. The silicone oil in the thermostat was constantly stirred and flowed to ensure the temperature uniformity. The precise temperature value was converted using the resistance value of the industry-standard platinum resistor.

In that the heating chip was too small and light to fix in the thermostat, a supporting device was designed to fix small heating chips in the bottom slot of the device. The standard platinum resistor was inserted into the tube from the top of the device to make the chips and the sensitive part of the resistor at the same depth in the thermostat, ensuring the consistency of temperature, as shown in Fig. 15.

2) FOUR-WIRE RESISTANCE MEASUREMENT

The common method of measuring resistance is two-wire measurement, with two wires connected to two ends of the resistor. The resistance is obtained by measuring the voltage across the resistor and the passing current. However, this method cannot eliminate the influence of the wire resistance. Therefore, four-wire resistance measurement method is adopted. The schematic is shown in Fig. 16. There are two leads at each ends of the resistor. Two of the leads provide a constant current converting the resistance into a voltage signal, which is measured by the other two leads.

The black box on the left side of Fig. 16 is the Agilent 34410A digital multimeter. The internal resistance of the voltmeter is very high on account of the internal amplifier. Therefore, the current flowing through the voltmeter loop is extremely small, so that the voltage drop caused by the wire resistance on this loop can be ignored. This method eliminates the effect of wire resistance and improves measurement accuracy.

FIGURE 15. Supporting device and thermostat.

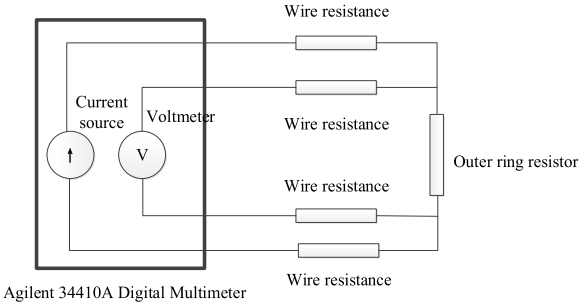

FIGURE 16. Four-wire measurement schematic.

3) TEMPERATURE CORRECTION

The thermostat was set to 60,80,100, and 120°C to obtain the resistance calibration data. A standard platinum resistance was used to obtain accurate temperature value.

Because standard platinum resistors have different slight deviations from the product design, there is a qualification certificate for each standard platinum resistor containing temperature correction parameters. For example, the temperature difference of the thermostat deviating from 60°C is measured by the platinum thermometer with this formula:

$$\Delta t_{60}^{*} = \left(\frac{R_{60}^{*}}{R_{tp}^{*}} - dw - W_{60}^{S} \right) \Big/ \left(dW_t^S / dt \right) \tag{7}$$

where R_{60}^{*} is the resistance value of the standard platinum resistance measured in a thermostat which is set to 60°C, R_{tp}^{*} is the resistance value at water triple point, W_{60}^{s} and $\left(\frac{dW_t^s}{dt}\right)_{t=60}$ are parameters given in the standard platinum resistance qualification certificate. dw is a corresponding

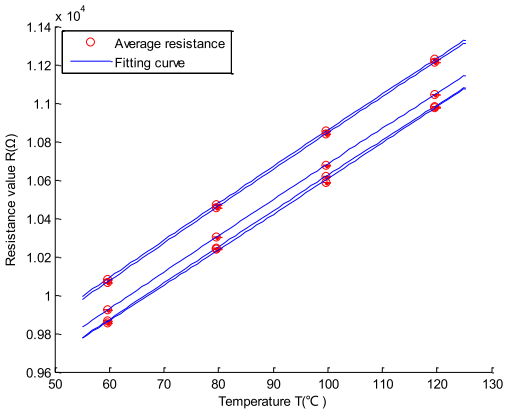

FIGURE 17. Resistance change with temperature and the fitting curve.

correction factor:

$$dw = a \times \left(\frac{R^*_{60}}{R^*_{tp}} - 1\right) + b \times \left(\frac{R^*_{60}}{R^*_{tp}} - 1\right)^2 \tag{8}$$

where a, b are also parameters given in the qualification certificate. So, the accurate temperature value is $t_{60} = 60 + \Delta t^*_{60}$.

4) RESULTS

At each temperature point, positive and negative currents were applied for 4 times to attenuate the effects of thermoelectric power. 30 resistances were recorded each time. So that each resistor has 120 data points at each temperature point including each heating chip and the standard platinum resistor. The average value and the standard deviation of the remaining data were calculated, as Fig. 17 shows.

For each platinum resistor, the relationship between the resistance and the temperature is fitted by a quadratic function:

$$R_t = A + B \times t + C \times t^2 \tag{9}$$

where A, B, and C are the constant coefficient, the coefficient of the 1st order term and the coefficient of the 2nd order term.

The temperature coefficient of resistance (TCR) is defined as:

$$\alpha = \frac{R_{100} - R_0}{R_0 \times 100} \tag{10}$$

The temperature coefficient and parameters of fitting formula the of each resistor where A, B, and C are the constant coefficient, the coefficient of the 1st order term and the coefficient of the 2nd order term are listed in Table 2.

The higher TCR, the more sensitive the resistor is to temperature changes. The TCR of the temperature measurement coil on the heating chip is smaller than the standard platinum resistance of 0.39%, due to the small thickness of Pt coil deposited by PECVD and the mutual diffusion of metal Pt with Ti adhesion layer.

TABLE 2. TCR and parameters of fitting formula of 5 resistors.

No.	TCR/ %/°C	A	B	C
1	0.22166	8696.479	20.118	-0.008414
2	0.22166	8745.396	20.220	-0.008355
3	0.22218	8885.848	20.611	-0.008682
4	0.22302	8867.582	20.645	-0.008682
5	0.20650	8790.951	17.634	0.0051956

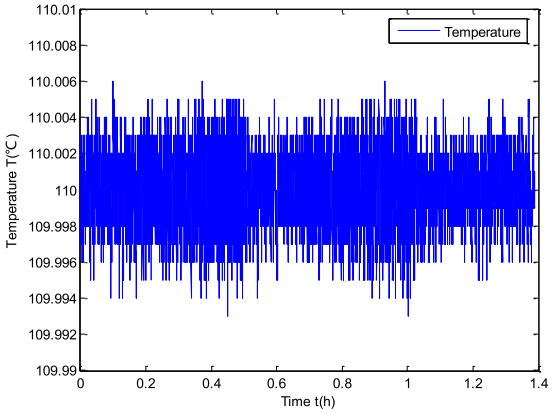

FIGURE 18. Curve of local temperature controlled by heating chip in 1.4 hours.

C. TEMPERATURE CONTROL

The NI board for impedance measurement was used to measure the resistance value of the temperature sensing coil, and a LabVIEW program performed PID control to the voltage amplitude of the heating resistance wire to adjust the temperature accurately. The local temperature of the outer coil during a period of 1.4 h is shown in Fig. 18. The temperature of the coil was stabilized to 110 °C, and the deviation is only within 10 mK.

D. MAGNETIC TEST

A commercial magnetometer was used to test the magnetic flux density generated by the heating chip. The heating chip was placed close to the magnetometer package. An alkali metal vapor cell, working as the sensitive component of the magnetometer, is about 7mm away from the edge of the outer casing.

1) MAGNETIC FLUX DENSITY SIMULATION

The magnetic flux density in a 6 mm cube around the cell is calculated. The simulation model is as Fig. 19 shows, the coordinate of the cell relative to the heating chip is X = 0 mm, Y = 0 mm, Z = 7 mm.

All wires were considered in simulation, including the wires of the MEMS heating chip, the gold wires for connection, and the wires on the substrate board. Because real coils include arc sections and straight line sections, (11) and (12) expressing the magnetic flux densSities at the position of (x, y, z) generated by an arc wire and a straight wire according

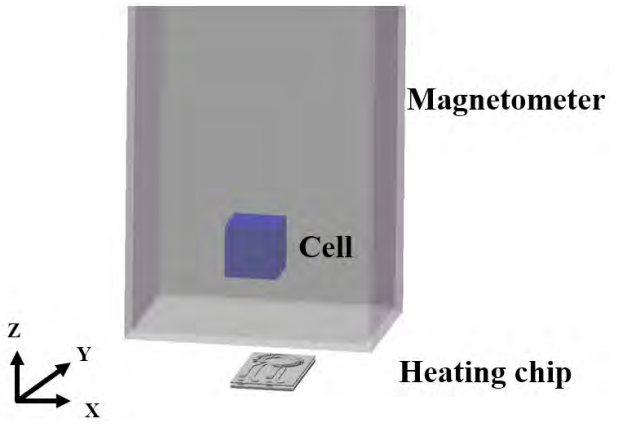

FIGURE 19. Simulation model diagram.

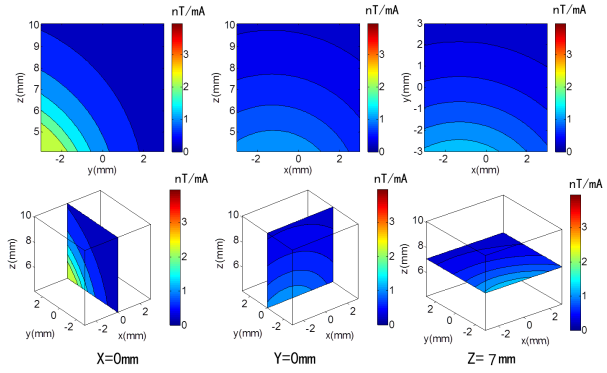

FIGURE 20. Magnetic flux density on the plane of $X = 0$ mm, $Y = 0$ mm, $Z = 7$ mm.

to the Biot-Savart Law, were calculated.

$$B_{arc}(x,y,z) = \int_{-\frac{\Phi}{2}}^{\frac{\Phi}{2}} \frac{\frac{\mu_0 NI}{4\pi}}{(x-\frac{D\cos\varphi}{2})^2+(y-\frac{D\sin\varphi}{2})^2+(z+\frac{h}{2})^2} \cdot \begin{bmatrix} \vec{i} & \vec{j} & \vec{k} \\ -\frac{D\sin\varphi}{2}d\varphi & \frac{D\cos\varphi}{2}d\varphi & 0 \\ x-\frac{D\cos\varphi}{2} & y-\frac{D\sin\varphi}{2} & z+\frac{h}{2} \end{bmatrix} \quad (11)$$

$$B_{str}(x,y,z) = \int_{-\frac{h}{2}}^{\frac{h}{2}} \frac{\frac{\mu_0 NI}{4\pi}}{(x-\frac{D\cos\varphi}{2})^2+(y-\frac{D\sin\varphi}{2})^2+(z-z')^2} \cdot \begin{bmatrix} \vec{i} & \vec{j} & \vec{k} \\ 0 & 0 & dz' \\ x-\frac{D\cos\frac{\varphi}{2}}{2} & y-\frac{D\sin\frac{\varphi}{2}}{2} & z-z' \end{bmatrix} \quad (12)$$

Three figures show the magnetic flux density distribution in the planes of X = 0 mm, Y = 0 mm, Z = 7 mm. The 4 mm cube cell is located in the center of the simulation range which is 6 mm cube around the cell. Most magnetic flux density in the cell area caused by the unit current in the heating chip are lower than 1 nT/mA, as shown in Fig. 20, showing the double-layer winding structure has significant magnetic flux density suppression effect.

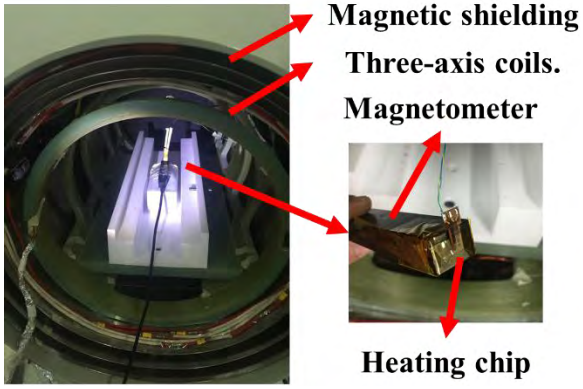

FIGURE 21. Photograph of experimental devices.

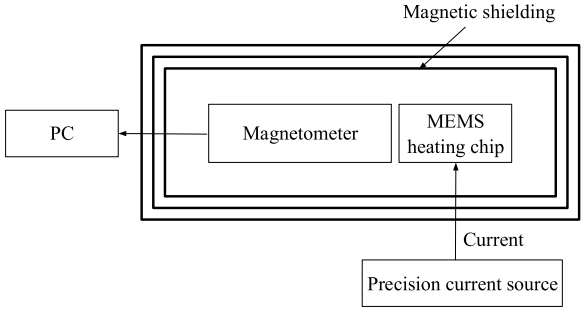

FIGURE 22. Experimental setup of DC magnetic flux density test.

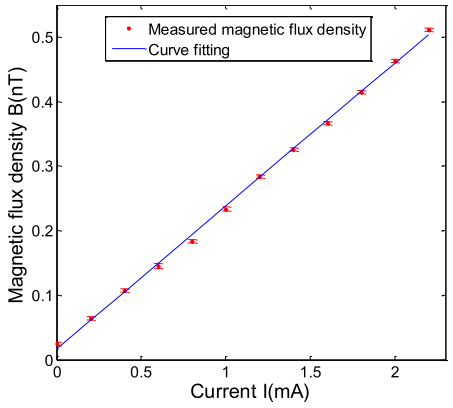

FIGURE 23. Magnetic flux density by heating chip with DC current.

2) DC MAGNETIC FLUX DENSITY TEST

In the experiment, the MEMS heating chip and the magnetometer were fixed in a magnetic shielding, which could suppress the interference of the geomagnetic flux density from 100000 nT to several nT. Residual magnetic flux density was compensated to several fT by preset three-axis coils, as shown in Fig. 21.

The precision current source generated different current from 0 to 2.2 mA with interval of 0.2 mA for the MEMS heating chip. When the state was stable, the magnetometer measured the magnetic flux density generated by the heating chip in the Z direction, correspondingly. Under each current, 600 points of data were obtained.

The mean values and variances corresponding to the current are drawn in Fig. 23, whereas the variance is not obvious

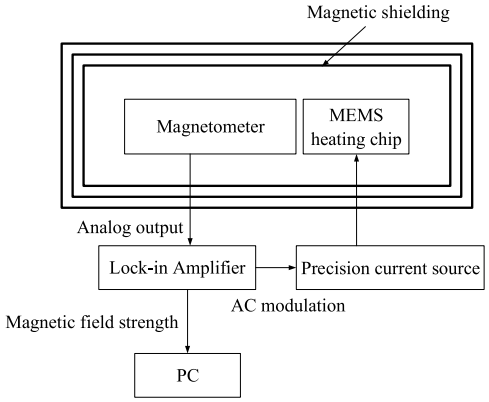

FIGURE 24. Experimental setup of AC magnetic flux density test.

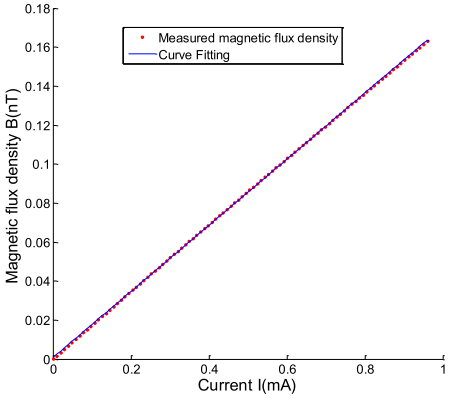

FIGURE 25. Measured magnetic flux density by AC current.

because of good data repeatability. The data is fitted to a straight line expressed by

$$B = 0.2215 \times I + 0.0167 \tag{13}$$

Therefore, the magnetic flux density generated by the heating chip in the Z direction is 0.2215 nT/mA. The regression coefficients is 0.9988.

3) AC MAGNETIC FLUX DENSITY TEST

As it is hard to avoid the drift of magnetic flux density and low frequency interference in DC test. In order to reduce these errors, a lock-in amplifier modulating the precision current source was utilized to provide a fixed frequency sine wave current, as shown in Fig. 24.

The amplitude of modulated precision current source was from 0 to 1 mA with an interval of 0.01 mA. The analog output from the magnetometer was demodulate by the lock-in amplifier to obtain the corresponding magnetic flux density strength in the Z direction.

The data of mean values is fitted to a straight line as Fig. 25 shows. The fitted equation is expressed by

$$B = 0.1696 \times I + 0.0008 \tag{14}$$

The magnetic flux density generated by the heating chip in the Z direction is 0.1696 nT/mA. The regression coefficients is 0.999948, which is much better than that in the DC magnetic flux density test.

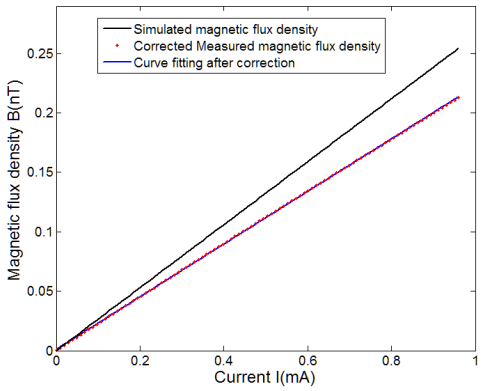

FIGURE 26. Measured and simulated magnetic flux density strength in the Z direction.

Due to the bandwidth limitations of the magnetometer, the signal response of the AC test is lower than the response of DC test, proportionally to frequency-related coefficient K_f.

$$S_{AC} = K_f \cdot S_{DC} \tag{15}$$

In this case, $K_f = S_{AC}/S_{DC} = 1.3054$. It is necessary to correct each AC test data by multiplying Kf.

The cell center of the commercial magnetometer is about 7 mm from the heating chip. The simulation results at z = 7 mm shows the magnetic flux density generated by the MEMS heating chip in the Z direction is 0.2652 nT/mA, as shown in Fig. 26.

Difference between simulation results and test results may be caused by the following reasons: Firstly, the position of the magnetometer in the test is not exactly the same as in the simulation. Secondly, the magnetic flux density measured by the magnetometer is the average of the cell, not the value of a single point in the simulation. At last, the irregular gold wire model cannot be simulated extremely accurately.

IV. CONCLUSION

A small-sized MEMS heating chip for the temperature control of cell in the SERF magnetometer was designed and fabricated in this paper. The magnetic flux density simulation verified the necessity of the double-layer heating film. In the fabrication process, two layers of metal can be effectively connected to realize a double-layer meander structure, achieving magnetic flux density suppression, significantly reducing the magnetic noise introduced by the heating current. Comparing with the single-layer heating film, the double-layer heating film can reduce the magnetic noise introduced by the heating current by more than 4 orders of magnitude. The resistance consistency of fabricated resistors is better than 97.7%, and the temperature coefficient of resistance can reach 0.224%/°C. The fluctuation of temperature at 110 °C is under 10 mK. The magnetic flux density introduced by the current in the Z direction is 0.22146 nT/mA. With a highly integrated package, the proposed MEMS heating chip can integrate temperature measurement and heating function

to control the temperature of gas cell, which lays a foundation for the miniaturization of quantum sensing instruments.

REFERENCES

[1] D. Robbes, "Highly sensitive magnetometers—A review," *Sens. Actuators A, Phys.*, vol. 129, no. 1, pp. 86–93, Jan. 2006.

[2] C. Johnson, N. L. Adolphi, K. L. Butler, M. L. Debbie, R. Larson, P. D. Schwindt, and E. R. Flynn, "Magnetic relaxometry with an atomic magnetometer and squid sensors on targeted cancer cells," *J. Magn. Magn. Mater.*, vol. 324, no. 17, pp. 2613–2619, Mar. 2012.

[3] A. Guedes, R. Macedo, G. Jaramillo, S. Cardoso, P. P. Freitas, and D. A. Horsley, "Hybrid GMR sensor detecting 950 pT/sqrt(Hz) at 1 Hz and room temperature," *Sensors*, vol. 18, no. 3, p. 790, Mar. 2018.

[4] E. Boto, S. S. Meyer, V. Shah, O. Alem, S. Knappe, P. Kruger, T. M. Fromhold, M. Lim, P. M. Glover, P. G. Morris, R. Bowtell, G. R. Barnes, and M. J. Brookes, "A new generation of magnetoencephalography: Room temperature measurements using optically-pumped magnetometers," *NeuroImage*, vol. 149, no. 1, pp. 404–414, Apr. 2017.

[5] D. Budker and M. Romalis, "Optical magnetometry," *Nature Phys.*, vol. 3, no. 4, pp. 227–234, Apr. 2007.

[6] S. J. Seltzer, "Developments in alkali-metal atomic magnetometry," Ph.D. dissertation, Princeton Univ., Princeton, NJ, USA, 2008.

[7] S. Xing, D. Haifeng, and F. Jiancheng, "Chip scale atomic magnetometer based on SERF," in *Proc. 4th IEEE Int. Conf. Nano/Micro Eng. Mol. Syst. (IEEE-NEMS)*, Shenzhen, China, Jan. 2009, pp. 231–234.

[8] M. P. Ledbetter, I. M. Savukov, V. M. Acosta, M. V. Romalis, and D. Budker, "Spin-exchange-relaxation-free magnetometry with Cs vapor," *Phys. Rev. A, Gen. Phys.*, vol. 77, no. 3, May 2008, Art. no. 033408.

[9] J. H. Liu, D.-Y. Jing, L.-L. Wang, Y. Li, W. Quan, J.-C. Fang, and W.-M. Liu, "The polarization and the fundamental sensitivity of ^{39}K (^{133}Cs)-^{85}Rb-^{4}He hybrid optical pumping spin exchange relaxation free atomic magnetometers," *Sci. Rep.*, vol. 7, no. 1, Jul. 2017, Art. no. 6776.

[10] R. Wylie, "The development of a multichannel atomic magnetometer array for fetal magnetocardiography," Ph.D. dissertation, Univ. Wisconsin-Madison, Madison, WI, USA, 2012.

[11] V. Shah, S. Knappe, P. D. D. Schwindt, and J. Kitching, "Subpicotesla atomic magnetometry with a microfabricated vapour cell," *Nature Photon.*, vol. 1, pp. 649–652, Nov. 2007.

[12] G. Vasilakis, "Precision measurements of spin interactions with high density atomic vapors," Ph.D. dissertation, Princeton Univ., Princeton, NJ, USA, 2011.

[13] J. C. Allred, R. N. Lyman, T. W. Kornack, and M. V. Romalis, "High-sensitivity atomic magnetometer unaffected by spin-exchange relaxation," *Phys. Rev. Lett.*, vol. 89, no. 13, Sep. 2002, Art. no. 130801.

[14] J. M. Brown, "A new limit on lorentz-and CPT-violating neutron spin interactions using a K-^{3}He comagnetometer," Ph.D. dissertation, Dept. Phys., Princeton Univ., Princeton, NJ, USA, 2011.

[15] P. D. D. Schwindt, B. Lindseth, V. Shaha, and J. Kitching, and S. Knappe, "Chip-scale atomic magnetometer with improved sensitivity by use of the M_x technique," *Appl. Phys. Lett.*, vol. 90, no. 8, Feb. 2007, Art. no. 081102.

[16] M. D. Bulatowicz, "Temperature system with magnetic field suppression," U.S. Patent 8 138 760, Mar. 20, 2012.

[17] Q. Cai, Y.-C. Chen, N. F. DeNatale, and C. Tsai, "Development of a platinum resistance thermometer on the silicon substrate for phase change studies," *J. Micromech. Microeng.*, vol. 22, no. 8, pp. 85012–85018, Apr. 2012.

[18] F.-J. Chuang, "Structure of the sensing element of a platinum resistance thermometer and method for manufacturing the same," U.S. Patent 6 004 471, Dec. 21, 1999.

LIANG XIAOYANG received the B.Sc. degree in measurement and control technology and instrument from the School of Instrumentation and Optoelectronics Engineering, Beihang University, Beijing, China, in 2015, where he is currently pursuing the Ph.D. degree. His current research interest includes SERF magnetometer.

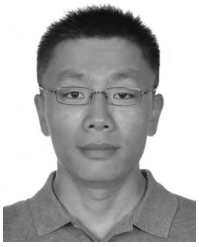

LIU ZHANCHAO received the B.Sc. and Ph.D. degrees in precision instrument and machinery from the School of Instrumentation and Optoelectronic Engineering, Beihang University, Beijing, China, in 2007 and 2015, respectively, where he is currently an Assistant Professor. His current research interests include SERF magnetometer, atomic gyroscope, inertial navigation, and integrated navigation.

DIE HU received the B.Sc. degree in measurement and control technology and instrument from the School of Instrument Science and Opto-Electronic Engineering, Beihang University, Beijing, China, in 2015, where she is currently pursuing the Ph.D. degree. Her current research interests include electrical tomography algorithms and tomography technology applications in flame monitoring.

WU WENFENG received the B.S. degree from the Tianjin University of Science and Technology, Tianjin, China, in 2012, and the M.S. degree from Shanghai University, Shanghai, China, in 2014. He is currently pursuing the Ph.D. degree with the school of Instrumentation Science and Optoelectronics Engineering, Beihang University, Beijing. His main research interests include the design of magnetic shield systems, nuclear magnetic resonance gyroscope, and atomic magnetometer.

JIA YUCHEN received the B.Sc. degree in measurement and control technology and instrument from the School of Instrumentation and Optoelectronics Engineering, Beihang University, Beijing, China, in 2016, where she is currently pursuing the Ph.D. degree. Her current research interests include SERF magnetometer and atomic gyroscope.

FANG JIANCHENG was born in Shandong, China, in 1965. He received the B.S. degree in electrical engineering from the Shandong University of Technology, Jinan, China, in 1983, the M.S. degree in automotive engineering from Xian Jiaotong University, Xi'an, China, in 1988, and the Ph.D. degree in mechanical engineering from Southeast University, Nanjing, China, in 1996. He is currently the Vice President of Beihang University, Beijing, China. He holds a Special Appointment Professorship with the title of Cheung Kong Scholar, which was jointly established by the Ministry of Education of China and the Li Ka Shing Foundation. He has authored or coauthored over 150 papers and four books. His current research interests include the attitude control system technology of spacecraft, novel inertial instrument and equipment technology, inertial navigation, SERF atomic magnetometer, and co-magnetometer.